Princeton Plasma Physics Laboratory

PPPL- 4988

PPPL- 4988

Linear Mode Conversion of Langmuir/z-mode Waves to Radiation In Plasmas With Various Magnetic Field Strength

Eun-Hwa Kim, et. al.

FEBRUARY, 2014

PPPL PRINCETON PLASMA PHYSICS LABORATORY

Prepared for the U.S. Department of Energy under Contract DE-AC02-09CH11466.

Princeton Plasma Physics Laboratory
Report Disclaimers

Full Legal Disclaimer

Trademark Disclaimer

PPPL Report Availability

Princeton Plasma Physics Laboratory:

http://www.pppl.gov/techreports.cfm

Office of Scientific and Technical Information (OSTI):

http://www.osti.gov/bridge

Related Links:

U.S. Department of Energy

Office of Scientific and Technical Information

Fusion Links

Linear mode conversion of Langmuir/z-mode waves to radiation in plasmas with various magnetic field strength

Eun-Hwa Kim (김은화),[1,a)] Iver. H. Cairns,[2,b)] and Jay R. Johnson[1,c)]
[1]*Plasma Physics Laboratory, Princeton University, Princeton, New Jersey 08543, USA*
[2]*School of Physics, University of Sydney, Sydney, New South Wales 2002, Australia*

(Received 22 July 2013; accepted 6 November 2013; published online 5 December 2013)

Linear mode conversion of Langmuir/z waves to electromagnetic radiation near the plasma and upper hybrid frequency in the presence of density gradients is potentially relevant to type II and III solar radio bursts, ionospheric radar experiments, pulsars, and continuum radiation for planetary magnetospheres. Here, we study mode conversion in warm, magnetized plasmas using a numerical electron fluid simulation code when the density gradient has a wide range of angle, δ, to the ambient magnetic field, $\mathbf{B}_0$, for a range of incident Langmuir/z wavevectors. Our results include: (1) Left-handed polarized ordinary (oL) and right-handed polarized extraordinary (xR) mode waves are produced in various ranges of δ for $\Omega_0 = (\omega L/c)^{1/3}(\omega_{ce}/\omega) < 1.5$, where ω_{ce} is the (angular) electron cyclotron frequency, ω is the angular wave frequency, L is the length scale of the (linear) density gradient, and c is the speed of light; (2) the xR mode is produced most strongly in the range, $40° < \delta < 60°$, for intermediately magnetized plasmas with $\Omega_0 = 1.0$ and 1.5, while it is produced over a wider range, $0° \leq \delta \leq 90°$, for weakly magnetized plasmas with $\Omega_0 = 0.1$ and 0.7; (3) the maximum total conversion efficiencies for wave power from the Langmuir/z mode to radiation are of order 50%–99% and the corresponding energy conversion efficiencies are 5%–14% (depending on the adiabatic index γ and $\beta = T_e/m_e c^2$, where T_e is the electron temperature and m_e is the electron) for various Ω_0; (4) the mode conversion window becomes wider as Ω_0 and δ increase. Hence, the results in this paper confirm that linear mode conversion under these conditions can explain the weak total circular polarization of interplanetary type II and III solar radio bursts because a strong xR mode can be generated via linear mode conversion near $\delta \sim 45°$. © *2013 AIP Publishing LLC*.
[http://dx.doi.org/10.1063/1.4837515]

I. INTRODUCTION

Standard linear analyses of dispersion relations for homogeneous plasmas yield wave modes that are uncoupled and distinct. However, in inhomogeneous plasmas, the wave modes are often coupled to each other. For some range of frequency and angle of propagation, the energy can be transformed linearly from one mode to another with constant frequency via a process called linear mode conversion (LMC).[1]

Density gradients facilitate LMC from the Langmuir/z mode into electromagnetic (EM) waves when the wave frequency is near the electron plasma frequency (ω_{pe}). This LMC process is potentially relevant to radiation from foreshock regions upstream of Earth's bowshock,[2,3] type II and III radio bursts from the solar corona and interplanetary medium[4–10] radiation from the outer heliosphere,[11] and ionospheric medium frequency bursts.[12] LMC also occurs near the upper hybrid resonance (ω_{UH}) and is believed to be important in producing continuum radiation in the magnetospheres of Earth and other magnetized planets,[13–17] and auroral roar emissions.[18]

Recent progress in LMC theory suggests that LMC can effectively generate solar and heliospheric emissions.[4–6] Kim *et al.*[4,5] (hereafter KCR08) demonstrated that LMC can produce the right-handed polarized extraordinary (xR) mode as well as the left-handed polarized ordinary (oL) mode from Langmuir/z waves, contrary to earlier expectations that restricted the mode conversion process to only the oL mode.[19] They suggested that the partially polarized type II and III radio bursts, which have degrees of polarization between 0% and 70%, but are never 100% polarized,[20] could be directly generated via the LMC process because the production of both xR- and oL-mode radiation by LMC leads immediately to weakly circularly polarized radiation. KCR08 also showed that the energy conversion efficiency, defined as the ratio between of energy densities for incoming Langmuir/z and outgoing EM waves, is similar to nonlinear and observed conversion efficiencies.

The angle between the density gradient and the background magnetic field (δ) varies from 0° to 90° in space. Continuum radiation from planetary magnetospheres is believed to come preferentially from a source near the magnetic equator.[13,21–25] There, the average density gradient (∇N_0) is approximately radial, and the background magnetic field ($\mathbf{B}_0$) is perpendicular to the magnetic equator, so $\delta = 90°$.[22,26] For type II and III bursts in the corona and solar wind and terrestrial foreshock emissions, ∇N_0 is directed radially outward from the Sun, while the direction of $\mathbf{B}_0$ with respect to the radial direction (density gradient) is $\delta \approx 45°$ (Refs. 8 and 26) at 1AU and increases beyond 1AU asymptoting to $\delta \approx 90°$ in the outer

[a)]Electronic address: ehkim@pppl.gov
[b)]Electronic address: cairns@physics.sydney.edu.au
[c)]Electronic address: jrj@pppl.gov

heliosphere, according to the Parker model for $\mathbf{B}_0$. However, most previous LMC studies for simplicity focused on parallel density cases where $\nabla N_0 \parallel \mathbf{B}_0$.[2,4,5,27,28] For the parallel case, LMC occurs near $\omega \sim \omega_{pe}$, where ω is the incoming wave frequency but in the perpendicular density case[29–32] where $\nabla N_0 \perp \mathbf{B}_0$ and LMC occurs near $\omega \sim \omega_{UH}$.

Recently, LMC for the case of oblique density gradients has been examined.[6] Using a warm plasma wave simulation code developed in Ref. 4, Schleyer *et al.*[6] (hereafter SCK13) calculated the mode conversion efficiencies in weakly magnetized plasmas. They showed that the energy conversion efficiency is strongly dependent on the angle δ, $\beta = T_e/m_e c^2$, where T_e is the electron temperature, m_e is the electron mass, and c is the speed of light, and the incident angle θ of Langmuir/z waves to the density gradient. They also showed that the power conversion efficiency, defined as the ratio between incoming and outgoing Langmuir wave power, is independent of β. However, they only adopted a single background magnetic field strength (B_0) and ratio $\omega_{ce}/\omega_{pe} = 0.005$, where ω_{ce} is the electron gyrofrequency, in a weakly magnetized plasma. Because both the mode conversion efficiencies and outgoing EM wave polarization depend on ω_{ce}/ω_{pe} (Refs. 4 and 5) and can vary substantially in strongly magnetized plasmas, it is necessary to investigate how wave polarizations and conversion efficiencies depend on $\mathbf{B}_0$ and δ.

The purpose of this paper is to investigate the LMC process as a function of δ, B_0, and θ and to examine the conversion efficiency from Langmuir/z to *oL* and *xR* waves, respectively. This paper provides an extension of the previous simulations and analyses of KCR08 and SCK13 into parameter regimes relevant to the entire heliosphere. We determine the power of the incoming and reflected Langmuir/z waves and the outgoing *oL* and *xR* modes from the simulated data and calculate the total, *oL* and *xR* modes' energy and power conversion efficiencies. We also construct the hodograms and polarization ellipses of outgoing EM waves and compare the results with theory.

This paper is structured as follows: In Sec. II, the definitions of the power and energy conversion efficiencies and the relationship between these conversion efficiencies are described. Section III describes the simulations model descriptions and presents simulation results for the conversion efficiencies and outgoing wave polarizations. The last section contains a brief discussion and the conclusions.

II. MODE CONVERSION EFFICIENCIES

A. Definitions of mode conversion efficiency

The mode conversion efficiency from one mode to another can be defined using wave energy density or power. The energy mode conversion efficiency (ε) is defined as the fraction of energy from the incoming Langmuir/z mode wave ($u^L{}_{in}$) converted into EM wave energy ($u^{EM}{}_{out}$)[5]

$$\varepsilon = \frac{u^{EM}_{out}}{u^{L}_{in}}, \tag{1}$$

where $u^{EM}_{out} = \sum_{i=x,y,z} |E_i|^2_{EM,out}$, $u^L_{in} = \sum_{i=x,y,z} |E_i|^2_{L,in}$, $|E_i|^2_{L,in}$, and $|E_i|^2_{EM,out}$ are the spatial power spectra of the Langmuir/z and transverse fields in the ith dimension, respectively. The power conversion efficiency (ε_p) is

$$\varepsilon_p = 1 - |R_L|^2 = 1 - \frac{S^L_{out}}{S^L_{in}} = 1 - \frac{u^L_{out}}{u^L_{in}}, \tag{2}$$

where S is the Poynting flux and R_L is the reflection coefficient of the Langmuir/z mode. If there is only one outgoing EM wave mode, then the relationship between ε and ε_p becomes[4–6]

$$\frac{\varepsilon_p}{\varepsilon} = \frac{v^{EM}_g}{v^L_g}, \tag{3}$$

where $v_g{}^{EM}$ and $v_g{}^L$ are group velocities of EM and Langmuir/z waves. For unmagnetized plasmas, the group velocity ratio ($|v_g{}^{EM}/v_g{}^L|$) between EM and Langmuir/z waves is reduced[5,6] to $|v_g{}^{EM}/v_g{}^L| \approx (\gamma\beta)^{-1/2}$, where γ is the adiabatic index, thus,

$$\frac{\varepsilon_p}{\varepsilon} \approx (\gamma\beta)^{-\frac{1}{2}}. \tag{4}$$

In magnetized plasmas, there are two different outgoing EM waves (i.e., *oL* and *xR* waves) and the total energy conversion efficiency can be described as the sum of the *oL* (ε^-) and *xR* (ε^+) conversion efficiencies

$$\varepsilon \sim \varepsilon^+ + \varepsilon^-, \tag{5}$$

where the superscripts $\pm$ represent *xR* and *oL* mode waves, respectively. The relationship between ε_p and ε is

$$\varepsilon_p = 1 - |R_L|^2 \sim \varepsilon^+ \frac{v^+_g}{v^L_g} + \varepsilon^- \frac{v^-_g}{v^L_g}. \tag{6}$$

Equation (6) clearly shows that the relationship between ε and ε_p in strongly magnetized plasmas is not as simple as for unmagnetized or weakly magnetized plasmas, because $v_g{}^{\pm}$ is a function of B_0, N_0, γ, β, and wavevector, $\mathbf{k}$. In weakly magnetized plasmas, the ratio between the two conversion efficiencies reduces to Eq. (3) since $v_g{}^+ \sim v_g{}^- \approx kc^2/\omega$.

B. Parameters for conversion efficiency

The mode conversion efficiency is expected to be primarily a function of the quantities[28,33]

$$q = (k_0 L)^{2/3} \sin^2 \theta^L_{in} \tag{7}$$

and

$$\Omega_0 = (k_0 L)^{1/3} Y_e^{1/2}, \tag{8}$$

where $k_0 = \omega/c$, L is the density scale length, $\theta^L{}_{in}$ is the incident angle of Langmuir/z waves to ∇N_0, and $Y_e = \omega_{ce}/\omega$. Willes and Cairns[34] generalized Eq. (7) and found that the mode conversion efficiency is primarily a function of

$$q = (k_0 L)^{2/3} K^2_\perp, \tag{9}$$

where $K_\perp = k_\perp/k_0$ is the normalized wavevector perpendicular to ∇N_0 of the incoming Langmuir/z waves.

Similar to KCR08 and Ref. 34, the maximum of $\theta^L{}_{in}$ for outgoing oL and xR waves ($\theta^{L\pm}{}_{\text{max-}in}$) can be calculated from $K^2{}_\perp = (K^L \sin\theta^{L\pm}{}_{in})^2 = (K^\pm \sin\theta^\pm{}_{out})^2$, where $K^\pm$ are normalized wave numbers and $\theta^\pm{}_{out}$ is the angle between $K^\pm$ and ∇N_0 of outgoing oL ($-$) and xR ($+$) waves. Because the maximum of $\sin\theta^\pm{}_{out}$ is 1

$$\theta^{L\pm}_{\text{max}-in} = \sin^{-1}\left(\frac{K^\pm}{K^L}\right) \approx \sin^{-1}\left(\sqrt{\frac{\gamma\beta}{1-X_e}}K^\pm\right), \tag{10}$$

where $K^\pm = K^\pm$ ($\theta^\pm{}_{out} = 90°$), $(K^L)^2 = (1 - X_e)/(\gamma\beta)$ is the normalized wave numbers of the Langmuir/z mode and $X_e = (\omega_{pe}/\omega)^2$. For $\theta^\pm{}_{out} = \pi/2$, since outgoing oL and xR waves propagate perpendicular to ∇N_0, the angle between wavevector to $\mathbf{B}_0$ becomes $|\pi/2-\phi|$ (for instance, 90° for $\mathbf{B}_0 || \nabla N_0$ and 0° for $\mathbf{B}_0 \perp \nabla N_0$). Because EM waves far from the resonance cone in warm plasmas can be treated as cold plasma waves,[35] $K^\pm$ for outgoing EM waves in the region far from the mode conversion area can be calculated using the Appleton-Hartree equation[21] under the cold plasma approximation,

$$\left(K^\pm\right)^2 \approx 1 - \frac{X_e(1-X_e)}{1 - X_e - \frac{Y_e^2\sin^2|\pi/2-\phi|}{2} \pm \sqrt{\frac{Y_e^4\sin^4|\pi/2-\phi|}{4} + Y_e^2(1-X_e)^2\cos^2|\pi/2-\phi|}}. \tag{11}$$

From Eq. (7), (10), and (11), the maximum of q then can be calculated as

$$q^\pm_{\text{max}-in} = (k_0L)^{2/3}\left(\sqrt{\frac{1-X_e}{\gamma\beta}}K^\pm\right)^2. \tag{12}$$

Figure 1 shows $\theta^{L\pm}{}_{\text{max-}in}$ and $q^\pm{}_{\text{max-}in}$ as a function of Ω_0 for $\omega_{pe} = 2\times10^5\,\text{s}^{-1}$, $k_0L = 1\times10^3$, $\gamma\beta = 0.01$, $X_e = 0.95$, and $\delta = 0°$, 30°, 60°, and 90°, respectively. In this figure, $\theta^-{}_{\text{max-}in}$ for oL waves clearly increases when δ and/or Ω_0 increase, and $\theta^-{}_{\text{max-}in}$ always exceeds 0°. For $\delta = 0°$, $\theta^L{}_{\text{max-}in}$ does not depend on Ω_0 because the dispersion of two oL modes in Eq. (11) can be reduced to $K^2 = 1 - X_e$, which is independent of B_0. For the xR mode, $\theta^+{}_{\text{max}}$ has a maximum value of 5.74° near $\delta = 0°$ for $\gamma\beta = 0.01$ and decreases when δ and/or Ω_0 increases. The maximum value of Ω_0 for mode-converted xR-mode waves, which occurs when $q^+{}_{\text{max}} = 0$ and $\theta^+{}_{\text{max}} = 0°$, can be derived from Eqs. (8) and (11) when $K^+{}_\perp \to 0$ and $Y_e = (1–X_e)$, thus, $\Omega_0 \sim (k_0L)^{1/3}(1-X_e)^{1/2} = 2.24$ for the given conditions.

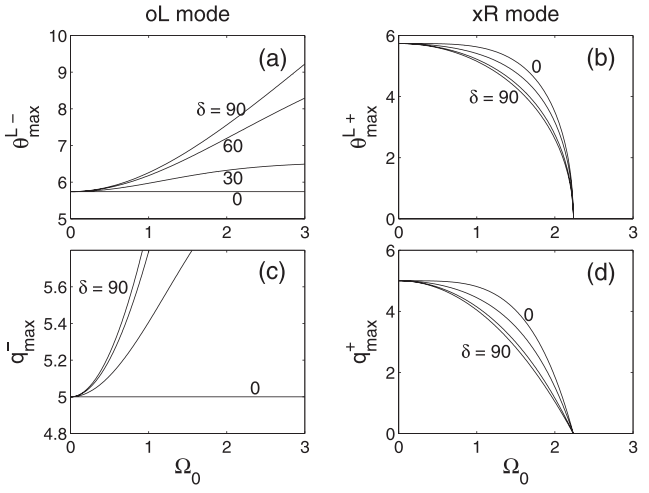

FIG. 1. The maximum angles $\theta = \theta^\pm{}_{\text{max-}in}$ in degrees and maximum values of $q = q^\pm{}_{\text{max-}in}$, where the superscripts $\pm$ represent xR and oL mode waves, respectively, for LMC into ((a) and (c)) the oL and ((b) and (d)) xR modes as functions of $\Omega_0 = (k_0L)^{1/3}Y^{1/2}$ for $k_0L = 1\times10^3$, $\gamma\beta = 0.01$, and $X_0 = 0.95$. Here, δ is the angle between density gradient and the ambient magnetic field.

Based on $\theta^\pm{}_{\text{max-}in}$ we can determine whether oL- and/or xR-mode waves can be generated from the Langmuir/z waves or not. Both oL and xR modes can be produced by LMC when $\theta^L < \theta^+{}_{\text{max}} < \theta^-{}_{\text{max}}$, but only the oL mode can be generated for $\theta^+{}_{\text{max}} < \theta^L < \theta^-{}_{\text{max}}$, while no EM waves can be produced for $\theta^L > \theta^-{}_{\text{max}}$. We examine wave simulations described in Sec. III for $0° \le \delta \le 90°$, $\Omega_0 < 2$, and $0.01 \le q \le 3.5$, respectively. In the simulations, the adopted values of q are lower than the values of $q^+{}_{\text{max-}in}$ in Figure 1 so that both oL and xR modes can be generated from Langmuir/z waves via the LMC process.

III. NUMERICAL SIMULATIONS

A. Model description

To investigate LMC between Langmuir/z and EM waves in warm magnetized plasmas we use the numerical fluid simulation code developed in Ref. 4. Assuming the plasma obeys an adiabatic pressure law with $PN^{-\gamma} = \text{constant}$, where P and N are the plasma pressure and density, respectively, the code solves the linearized Maxwell equations, the electron momentum and continuity equations for an electron fluid with finite mass and thermal pressure, and Ohm's law

$$\nabla \times \mathbf{E} = -\frac{\partial \mathbf{B}}{\partial t}, \tag{13}$$

$$\nabla \times B = \mu_0\mathbf{J} + \frac{1}{c^2}\frac{\partial \mathbf{E}}{\partial t}, \tag{14}$$

$$N_0 m_e \frac{\partial \mathbf{v}}{\partial t} = -N_0 e(\mathbf{E} + \mathbf{v}\times\mathbf{B}_0) - ne\mathbf{E}_0 - \nabla p - \nu\mathbf{v}, \tag{15}$$

$$\mathbf{J} = -N_0 e\mathbf{v}, \tag{16}$$

$$\frac{\partial n}{\partial t} = -\nabla \cdot (N_0 \mathbf{v}), \tag{17}$$

$$P = \gamma n P_0 / N_0, \tag{18}$$

$$P_0 = T_0 N_0, \tag{19}$$

and

$$\mathbf{E}_0 = -\frac{\nabla P_0}{N_0 e}. \tag{20}$$

Here, **E**, **B**, **v**, and **J** are the perturbed electric and magnetic fields, electron velocity, and current density, n and p are the perturbed electron density and pressure, and P_0, $\mathbf{E}_0$, and ν are the background electron pressure, magnetic fields, and collisional frequency, respectively. Since we have adopted a constant B_0 in slab geometry, there is no background electron velocity and current in the simulation. In addition, ν is only adopted near the boundary to absorb waves. Note that only linear perturbations are contained in Eqs. (13)–(20).

In order to solve equations numerically, the following assumptions are adopted:

1. We assume that ∇N_0 lies in the z direction and $\mathbf{B}_0 = (B_0 \sin\delta,\ 0,\ B_0 \cos\delta)$, where δ is the angle between $\mathbf{B}_0$ and ∇N_0. For simplicity, B_0 is assumed to be constant. We perform wave simulations for $\Omega_0 = 0.1$–2.0.
2. We define $X_e = \omega^2_{pe}/\omega^2$ with

$$X_e(Z) = \begin{cases} X_0 & \text{for } Z \le 0 \\ X_0(1 + Z/L) & \text{for } Z > 0, \end{cases} \tag{21}$$

where $X_0 = X_e\,(Z=0) = \omega^2_{p0}/\omega^2$ and $Z = k_0 z$ is a normalized length. Typical solar wind values for the electron density, with $\omega_{p0} = 2 \times 10^5\ \mathrm{s}^{-1}$and density scale length with $k_0 L = 1 \times 10^3$ are used. However, in order to save computing time, we assume that $\gamma\beta = 0.01$ rather than more plausible values of 10^{-4}–10^{-5} for the corona and solar wind. Here, we also assumed $X_0 = 0.95$ similar to the previous simulation studies.[4–6] Although both power and energy conversion efficiencies depend on $\gamma\beta$,[6,36] the simulation results for both the conversion efficiency and conversion window can be scaled to realistic parameter and the dependence of γ is weak compared to the dependence on β.[6] Thus, we adopt $\gamma = 1$, for simplicity. Under given conditions, mode conversion occurs near $Z_{\mathrm{mc}} = k_0 L\,(1 - X_0) = 50$ when $\omega \approx \omega_{pe}$.
3. Since collisions are adopted only near the boundary, plasma in the region where mode conversion occurs in the simulation box can be considered collisionless.
4. Because there is no background gradient in the X and Y direction, all variables may be represented as a superposition of Fourier modes with dependence, $\mathbf{A} = A(Z, t)\ \exp(iK_x X)$, where X and K_x are normalized lengths and wavenumbers: $X = k_0 x$ and $K_x = k_x/k_0$. Here, K_x is constant by Snell's law, and we assume $K_y = 0$ without loss of generality.
5. We divided the simulation box into four regions (see Figure 2 in Ref. 5); region I has constant N_0 but waves are damped due to imposition of collisions, region II has constant N_0 where Langmuir/z modes are generated in electric fields, region III has constant N_0, and region IV has inhomogeneous N_0, where mode conversion occurs. Although reflecting boundary conditions are used in the code, the waves damp before they reach the boundary in region I due to collisions so the boundary condition is effectively an outgoing boundary. Moreover, waves never reach the boundary in region IV because they are reflected and/or mode converted before they region that boundary.
6. The size of each region in the simulation box is arbitrary: $Z_{\mathrm{I}} = 80\lambda^L k_0$, where $\lambda^L = 2\pi c\sqrt{\gamma\beta}(\omega_0^2 - \omega_{p0}^2)^{-1/2}$ is wavelength of Langmuir wave in unmagnetized plasma, for region I, $Z_{\mathrm{II}} = 10\lambda^L k_0$ for region II, $Z_{\mathrm{III}} = 50$, 250, or $650\lambda^L k_0$ for region III, and $Z_{\mathrm{IV}} = 100\lambda^L k_0 + Z_{\mathrm{mc}}$ for region IV, respectively. In order to describe short wavelength Langmuir/z waves as well as long wavelength EM waves, the spatial grid size dZ is chosen to be $\mathrm{d}Z = k_0\lambda^L/14$.
7. For weakly magnetized plasmas ($\Omega_0 = 0.1$ and 0.7), we adopt a short simulation box with $Z_{\mathrm{III}} = 50\lambda^L k_0$, but for intermediately magnetized plasmas, longer simulation boxes with $Z_{\mathrm{III}} = 650\lambda^L k_0$ and $250\lambda^L k_0$ are used for $\Omega_0 = 1.0$ and 1.5, respectively.
8. Initial Langmuir/z waves are generated continuously by driving the E_x and E_z components in region II with a wave having a single frequency ω and wavevector $\mathbf{K} = (K^L{}_x, 0, K^L{}_z) = (K^L \sin\theta^L{}_{in},\ 0, K^L \cos\theta^L{}_{in})$. Time histories of the electric and magnetic fields in region III are then recorded during the stationary time period, after the initial transients have died out.

B. Calculations of mode conversion efficiency

Calculations of the conversion efficiency from the simulation data require the wave power in each wave mode, obtained from the Fourier transform (in Z) of the wave solution in region III where the density is constant and decomposition into the normal modes is straightforward. In order to distinguish the two separate peaks of oL and xR waves in the Fourier-transformed K domain, the resolution $\delta K = 2\pi/Z_{\mathrm{III}}$ should be smaller than the difference in wavenumber of the two peaks, at least $\delta K \le |K^+{}_z - K^-{}_z|$. For weakly magnetized cases of $\Omega_0 = 0.1$ and 0.7, because $K^+{}_z \approx K^-{}_z$, δK becomes extremely small and Z_{III} should be infinite or extremely large to separate two wave modes. Therefore, in order to save computing time, we adopt a short simulation box with $Z_{\mathrm{III}} = 50\lambda^L k_0$. With the short simulation box, δK is not sufficiently small enough to separate the oL and xR modes and thus the power in the oL and xR modes cannot be determined directly from the simulation data. For the intermediate magnetized plasmas, we adopt a longer simulation domain satisfying $\delta K < |K^+{}_z - K^-{}_z|$, which enables us to calculate the separate mode conversion efficiencies for both the oL and xR wave modes.

Figure 2 shows the peaks in the power spectra for various magnetization conditions in shorter and longer simulation boxes. The spatial dependences of the EM waveforms from E_y (the ES waves have E_x and E_z field only) in the left column of Figure 2 show direct evidence for superposition of two EM wave modes for all Ω_0 cases. Since $K^-{}_z \approx K^+{}_z$ and

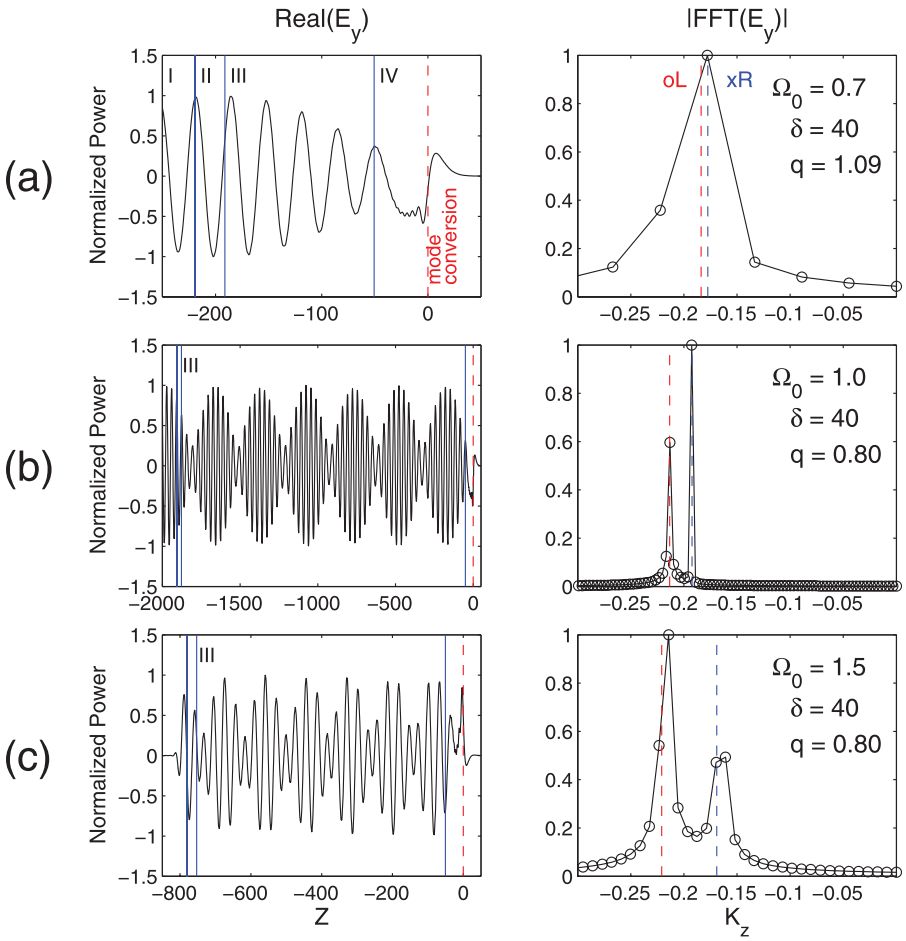

FIG. 2. (Left) Spatial dependence of real E_y, which is the pure EM wave modes for given conditions and (right) power spectra of complex E_y for (a) $\Omega_0 = 0.7$, $\delta = 40°$, and $q = 1.09$, (b) $\Omega_0 = 1.5$, $\delta = 40°$, and $q = 0.8$, and (c) $\Omega_0 = 1.5$, $\delta = 40°$, and $q = 0.8$, respectively. In the left columns, the abscissa is the Z direction and the ordinate is the normalized electric amplitude in arbitrary units. Simulation domains of regions I–IV are marked as blue dashed lines and the red dashed lines are where mode conversion occurs. In the right column, the power is also normalized in arbitrary units and the abscissa is normalized wavenumber $K_z = k_z/k_0$. The solid red and blue vertical lines are where $K_z = K_z^-$ and K_z^x, respectively.

$\delta K > |K^+{}_z - K^-{}_z|$ for $\Omega_0 = 0.7$, there is only one peak in the power spectra for $\Omega_0 = 0.7$ in Figure 2(a). However, two separated peaks of *oL* and *xR* waves are clearly seen in the right columns of Figures 2(b) and 2(c). The *xR* and *oL* mode waves are dominant for $\Omega_0 = 1.0$ and 1.5, respectively.

In order to calculate the energy of each of the wave modes, we adopt a wavenumber bandpass filter that covers the bandwidth $K^{\text{mode}} - \delta K \le K^{\text{mode}} \le K^{\text{mode}} + \delta K$, where K^{mode} is a center wavenumber of outgoing EM waves and $\delta K = 2\pi/Z_{\text{III}}$, and then we calculate the electric power of each mode according to

$$u^{\text{mode}} = \sum_j \sum_{2\delta K}^{K^{\text{mode}}+\delta K}_{K^{\text{mode}}-\delta K} \tilde{E}_j(K)\tilde{E}_j{}^*(K), \tag{22}$$

where $\tilde{E}$ is the bandpass-filtered Fourier transform of E in the spatial variable, Z. For the weakly case of $\Omega_0 = 0.1$ and 0.7, since $K^{\text{mode}} = K^+{}_z \approx K^-{}_z$ as shown in Figure 2(a), the peak in the total electric power contains both *oL* and *xR* waves. For the longer simulation box, the total electric power of the outgoing EM waves is sum of the power of the *oL* and *xR* waves

$$u_{out}^{EM} = u_{out}^- + u_{out}^+. \tag{23}$$

C. Simulation results: $\Omega_0 = 0.1$ and 0.7

For weakly magnetized plasmas with $\Omega_0 = 0.1$ and 0.7, we calculate the power (ε) and energy (ε_p) conversion efficiencies without separating into *oL* and *xR* modes and plot contours of ε and ε_p as a function of q and δ in Figure 3.

For $\Omega_0 = 0.1$ in Figures 3(a) and 3(b), both conversion efficiencies are independent of δ and are similar to the unmagnetized plasma cases[33,34] and the parallel density gradient case of $\delta = 0°$.[4,5] The maximum power ($\varepsilon_p{}^{\max}$) and energy ($\varepsilon^{\max}$) conversion efficiencies are $\varepsilon_p{}^{\max} \sim 50\%$ and $\varepsilon^{\max} \sim 5\%$, respectively, for those parameters. Owing to the weak $\mathbf{B}_0$, the ratio of the group speeds ($v_g{}^{\text{EM}}/v_g{}^{L}$) of the EM and Langmuir/z waves can be reduced to the unmagnetized plasma case of $(\gamma\beta)^{-1/2}$ in Eq. (2). Therefore, $\varepsilon_p/\varepsilon \sim 10 = (\gamma\beta)^{-1/2}$ for given conditions and the simulation results are in good agreement with theoretical ratios.

For $\Omega_0 = 0.7$ in Figures 3(c) and 3(d), both conversion efficiencies are shown maximize for the perpendicular density gradient ($\delta = 90°$, where $\varepsilon_p{}^{\max} \sim 80\%$ and $\varepsilon^{\max} \sim 8\%$) and minimize for parallel orientation ($\delta = 0°$, where $\varepsilon_p{}^{\max} \sim 40\%$ and $\varepsilon^{\max} \sim 4\%$), see also Ref. 6. The power (Δq_p) and energy (Δq) mode conversion q windows become wider when δ increases, which is similar to the previous simulation results of SCK13 for $\Omega_0 = 0.76$. In this case, the efficiency ratio, $\varepsilon_p/\varepsilon$, also can be reduced to the unmagnetized approximation, $\varepsilon_p/\varepsilon \sim 10 = (\gamma\beta)^{-1/2}$. We define a $q^{\max}$ (where $\varepsilon = \varepsilon^{\max}$) and $q_p{}^{\max}$ (where $\varepsilon_p = \varepsilon_p{}^{\max}$) for each δ. The value of $q^{\max}$ and $q_p{}^{\max}$ are almost constant as δ varies and $q^{\max} \approx q_p{}^{\max} \approx 0.5$ for both $\Omega_0 = 0.1$ and 0.7 in Figure 3.

By assuming that both the *oL* and *xR* modes are perfectly circularly polarized and analyzing hodograms in their

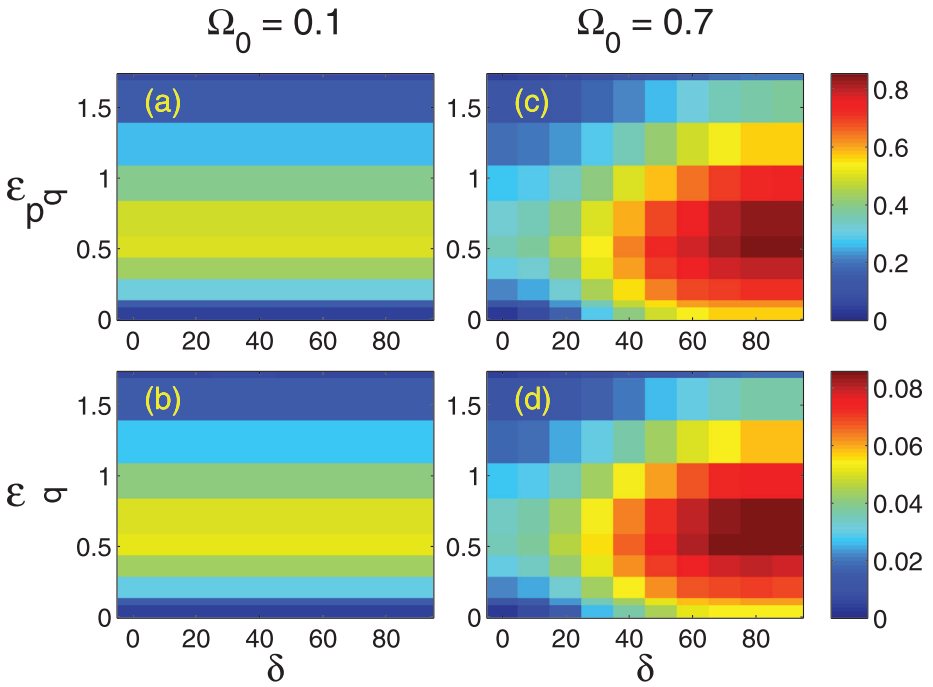

FIG. 3. Contour plot of the power (ε_p) and total energy (ε) conversion efficiencies in the q-δ plane for $X_0 = 0.95$, $\omega_{p0} = 2 \times 10^5\,s^{-1}$, $k_0L = 1 \times 10^3$, and $\gamma\beta = 0.01$ for (a) $\Omega_0 = 0.1$ and (b) 0.7.

simulations, KCR08 separated the total conversion efficiency into separate conversion efficiencies for the *oL* and *xR* waves for $\delta = 0°$. However, the *oL*- and *xR*- mode waves cannot be assumed to be 100% circularly polarized waves for $\delta \neq 0°$ even in weakly magnetized plasmas, and the method that KCR08 used is not appropriate. In addition, the homogeneous portion of the simulation domain chosen is too small to resolve the *oL* and *xR* mode conversion efficiencies directly for $\Omega_0 = 0.1$ and 0.7. Instead, we compose hodograms for the outgoing waves and compare them with the polarization ellipses analysis of the *oL* and *xR* modes.

In order to construct hodograms, we choose a single spatial point in region III and use a wavenumber bandpass filter to extract the pure long wavelength EM waves. This is because the long wavelength EM modes and short wavelength Langmuir/z waves have comparable amplitudes in both E_x and E_z. Then, the electric fields $\mathbf{E} = (E_x, E_y, E_z)$ are rotated to $(E_\perp, E_y, E_{||})$ with

$$\begin{pmatrix} E_\perp \\ E_{||} \end{pmatrix} = \begin{pmatrix} \cos\delta & -\sin\delta \\ \sin\delta & \cos\delta \end{pmatrix} \begin{pmatrix} E_x \\ E_z \end{pmatrix}, \tag{24}$$

where $E_{||(\perp)}$ is an electric field parallel (perpendicular) to $\mathbf{B}_0$.

In Figure 4, we plot hodograms of the polarization of the electric field transverse to $\mathbf{B}_0$ (i.e., $E_\perp$ and E_y) for (a) $\Omega_0 = 0.1$ and (b) 0.7, respectively. The columns are for $\delta = 20°$, $40°$, $60°$, and $80°$ and we choose a value of $q = 0.425$ that is close to q^{max} for all δ. The hodograms are normalized to the maximum value in each component so that a circularly polarized field would appear as a circle. The hodograms in Figure 4 confirm that in weakly magnetized plasmas both *oL* and *xR* wave modes are produced via LMC process in various δ, as explained in detail below.

Figure 4(a) shows that the sum of the EM waves for $\Omega_0 = 0.1$ are almost purely linearly polarized and that the polarization changes from linear to elliptical as δ increases. The ratios b/a of semi-major to semi-minor axes are 0, 0,

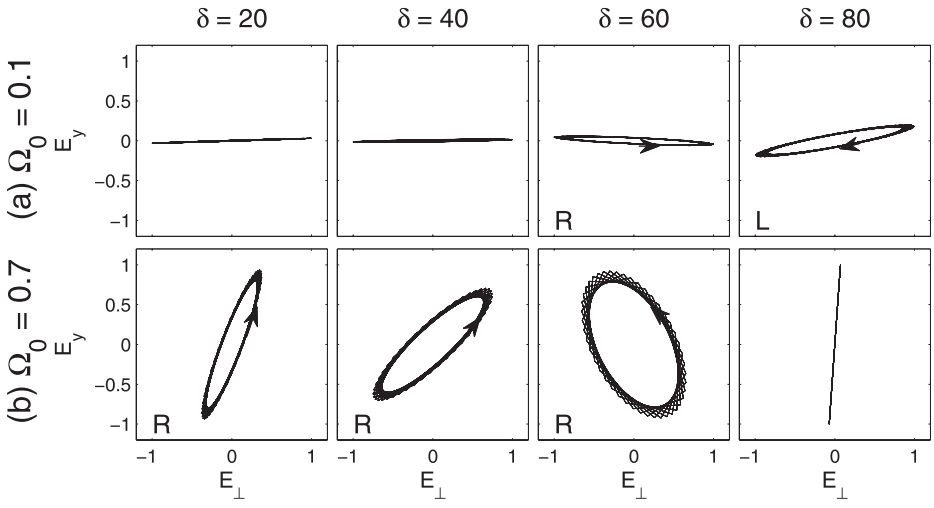

FIG. 4. Hodograms showing the polarization of the electric field transverse to $\mathbf{B}_0$ (i.e., $E_\perp$ and E_y) for (a) $\Omega_0 = 0.1$ and (b) 0.7. Columns represent for $\delta = 20°$, $40°$, $60°$, and $80°$, respectively.

0.03, and 0.08, while the theoretical ratios b/a of xR and oL wave modes are ± 0.8, ± 0.55, ± 0.23, and ± 0.12 for $\delta = 20°$, $40°$, $60°$, and $80°$, respectively, where $\pm$ represents xR and oL waves. Thus, the linear polarization for $\delta = 20°$ and $40°$, the right-handed elliptical polarization (RHP) for $\delta = 60°$, and left-handed elliptical polarization (LHP) for $\delta = 80°$ are evidence of the mixture of two EM wave modes.

For $\Omega_0 = 0.7$ in Figure 4(b), RHP and linear polarizations are dominant for $\delta = 0°$–$60°$ and $80°$, respectively. The ratios b/a are 0.14, 0.25, 0.53, and 0, for $\delta = 20°$, $40°$, $60°$, and $80°$, respectively, while the corresponding theoretical ratios b/a of the xR (oL) wave modes are ± 0.8, $0.57(-0.52)$, $0.27(-0.19)$, and $0.18(-0.08)$. Although the xR mode is dominant in this case, the simulated $|b/a|$ is much less (or more) than theoretical values because the outgoing EM waves are not 100% composed of xR waves but is a mixture of oL and xR waves. The results in Figure 4 are similar to wave simulations for $\delta = 0°$ that show linear polarized or RHP outgoing EM waves for $\Omega_0 < 1$.

D. Simulation results: $\Omega_0 = 1.0$ and 1.5

For intermediately magnetized cases, we adopt longer simulation boxes with $Z_{III} = 650\lambda^L k_0$ for $\Omega_0 = 1.0$ and $Z_{III} = 250\lambda^L k_0$ for $\Omega_0 = 1.5$, respectively. Since fine resolution of $\delta K = 2\pi/Z_{III}$ enables us to calculate the energy conversion efficiencies from Langmuir to oL and xR waves from the simulation data directly, we directly determine the power (ε_p), total energy (ε), Langmuir energy to oL-mode (ε^-), and Langmuir energy to xR-mode (ε^+) conversion efficiencies, respectively. These efficiencies are shown as a function of q and δ in Figure 5.

For $\Omega_0 = 1.0$ in Figures 5(a) and 5(b), ε_p and ε decrease compared to the value for $\Omega_0 = 0.7$ at small δ but increase for large δ. The minimum power and total energy conversion efficiencies occur near $\delta = 0°$ and the maximum conversion efficiencies increase up to $\varepsilon_p^{\max} \sim 95.5\%$ and $\varepsilon^{\max} \sim 12\%$ near $\delta \sim 60°$ and $q \sim 1.1$, as found in Ref. 6, while ε increases up to 4% for $(\Omega_0, \delta) = (0.7, 0°)$ and 8% for $(\Omega_0, \delta) = (0.7, 90°)$ in Figure 3. The minimum near $\delta = 0°$ is expected to be due to an interference effect between incoming and reflecting Langmuir/z waves, as shown in Ref. 5. Both ε and ε_p increase rapidly when δ increases from $0°$ to $60°$ but decrease slightly for $60° < \delta < 90°$. The value of $q_{(p)}^{\max}$ increases as δ increases and Δq_p becomes slightly wider.

Figures 5(c) and 5(d) plot the energy conversion efficiencies directly into oL (ε^-) and xR (ε^+) wave modes for $\Omega_0 = 1.0$. For most conditions of (δ, q) we determined ε^- and

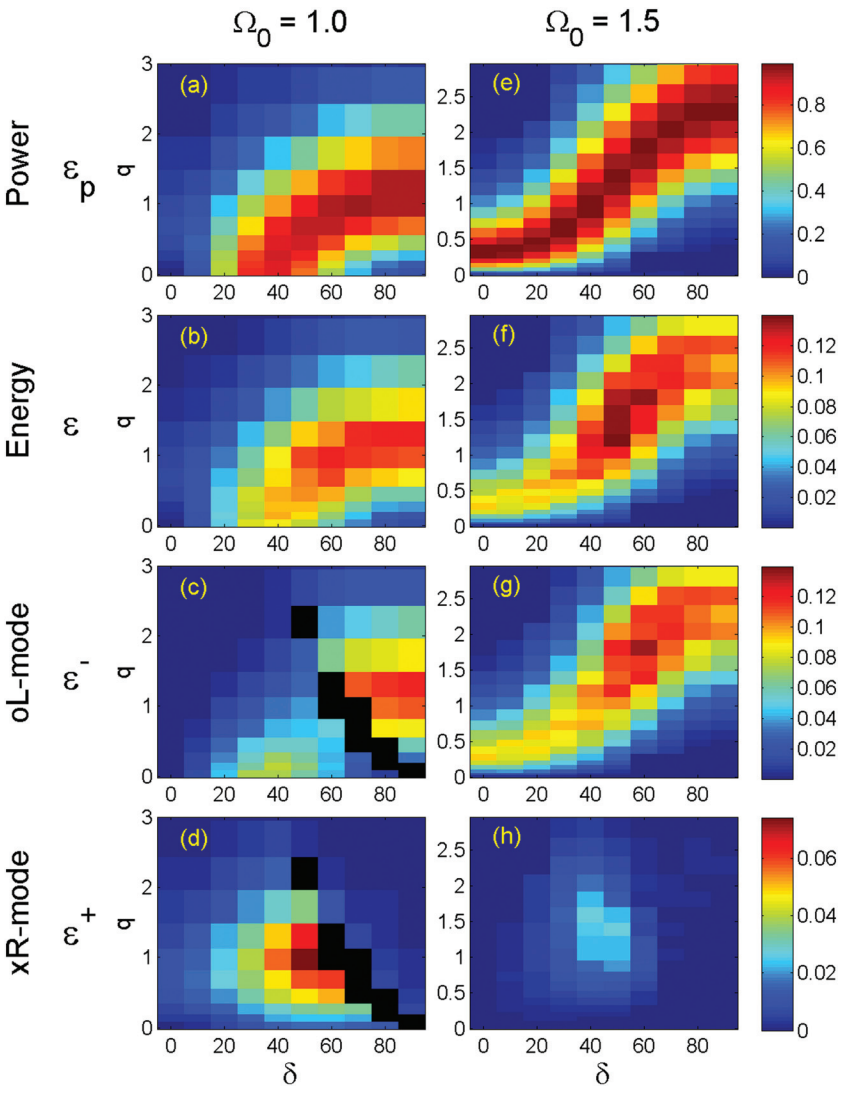

FIG. 5. Contour plot of the power conversion efficiency ε_p and the total energy (ε), oL-mode (ε^-), and energy to xR-mode (ε^+) conversion efficiencies in the q–δ plane for ((a)-(d)) $\Omega_0 = 1.0$ and ((e)-(h)) 1.5, respectively. Here, the black color represents regions where the oL and xR modes cannot be separated for each other due to the limited wavevector resolution of the simulations.

ε^+ directly from the simulation data; however, in the black regions in Figures 5(c) and 5(d), we can only calculate the total conversion efficiency ε because δK is not small enough to separate the two peaks.

For $\Omega_0 = 1.0$, ε^- is minimum near $\delta = 0°$ and increases with δ. For intermediate $40° < \delta < 60°$ and $0.5 < q < 1.5$, ε^- has a peak but does not exceed 46% of the maximum ε. At larger δ, ε^- increases significantly and has its overall maximum. The *oL* mode waves are dominant for large δ. In contrast to ε^-, ε^+ in Figure 5(d) shows the maximum near $\delta \sim 50°$ of about 7.4%.

For $\Omega_0 = 1.5$, ${\varepsilon_p}^{\max}$ in Figure 5(e) increases up to 99% for all δ and ${q_p}^{\max}$ increases as δ increases; thus, Δq_p shifts to higher q without changing ${\varepsilon_p}^{\max}(\delta)$ as δ increases. The width Δq for $\Omega_0 = 0.7$ increases as δ increases in Figure 3; however, $\varepsilon^{\max}$ also increases with δ. Different to ${\varepsilon_p}^{\max}$, $\varepsilon^{\max}(\delta)$ varies with δ as shown in Figure 5(f); $\varepsilon^{\max}$ peaks near $\delta = 50°$–$60°$ and $1.3 < q < 1.7$. The peak value $\varepsilon^{\max} \sim 14\%$ is higher than the value of 12% for $\Omega_0 = 1.0$. Figure 5(e) also shows that Δq slightly increases in δ.

For $\Omega_0 = 1.5$, the *oL* mode is dominant for all q and δ in Figures 5(g) and 5(h); the maximum of ε^- is 13.5% while the maximum of ε^+ is 2.7%. The only domain with significant ε^+ lies in the intermediate density gradient cases of $30° < \delta < 70°$, which is similar to the case $\Omega_0 = 1.0$ in Figure 5(d). Therefore, Figure 5 confirms that *xR*-mode waves can be generated from incoming Langmuir/*z* wave modes by LMC and that such radiation occurs effectively only for oblique density gradients and not for parallel or perpendicular density gradients.

In order to verify the relationship relates ε_p and ε in Eq. (6), in Figure 6, we plot the energy conversion efficiency $({\varepsilon_p}^c)$ for $\Omega_0 = 1.0$ and 1.5 that calculated from simulated $\varepsilon^{\pm}$ in Figure 5 and the theoretical ratio of group speed between EM and Langmuir/*z* waves $(v_g^{\pm}/v_g^L)$. The theoretical ratio of group speeds $v_g^{\pm}/v_g^L$ in Figures 6(a), 6(b), 6(d), and 6(e) clearly shows that $v_g^+ \neq v_g^-$ and strongly depends on $\mathbf{B}_0$, q, and δ. The value of ${\varepsilon_p}^c$ in Figures 6(c) and 6(f) increases over 100% under some conditions, but, in most cases, ${\varepsilon_p}^c$ agrees well with power conversion efficiencies. For instance, for $(\Omega_0, \delta, q) = (1.0, 50, 1.3)$, where ε is close to $\varepsilon^{\max}$, $v_g^-/v_g^L = 7.8$ and $v_g^+/v_g^L = 6.4$, and ${\varepsilon_p}^c$ is ~102% agreeing well with the simulation result of $\varepsilon_p \sim 99\%$.

E. Dependence on magnetic field strength

In Figures 3, 5, and 6, we found that the conversion efficiencies increase as Ω_0 increases. For instance, $\varepsilon^{\max}$ increases from 5% to 14% and ${\varepsilon_p}^{\max}$ increases from 50% to 99% as Ω_0 increases from 0.1 to 1.5. It is also found that $\Delta q_{(p)}$ becomes wider with increasing Ω_0 except for smaller δ. However, four cases of Ω_0 are not enough to determine how conversion efficiencies vary in Ω_0.

In order to investigate the detailed characteristics of how conversion efficiencies depend on B_0, we performed multiple simulations $0.1 < \Omega_0 < 2$. In these simulations, we adopt smaller $Z_{III} = 50\lambda^L k_0$ and wavenumber bandpass filter that covers bandwidth $K^+ - \delta K < K < K^+ + \delta K$ in order to contain both *oL* and *xR* waves. Figure 7 plots ε as a function of Ω_0 for $\delta = 0°$, 30°, 60°, and 90°, with blue, green, and red

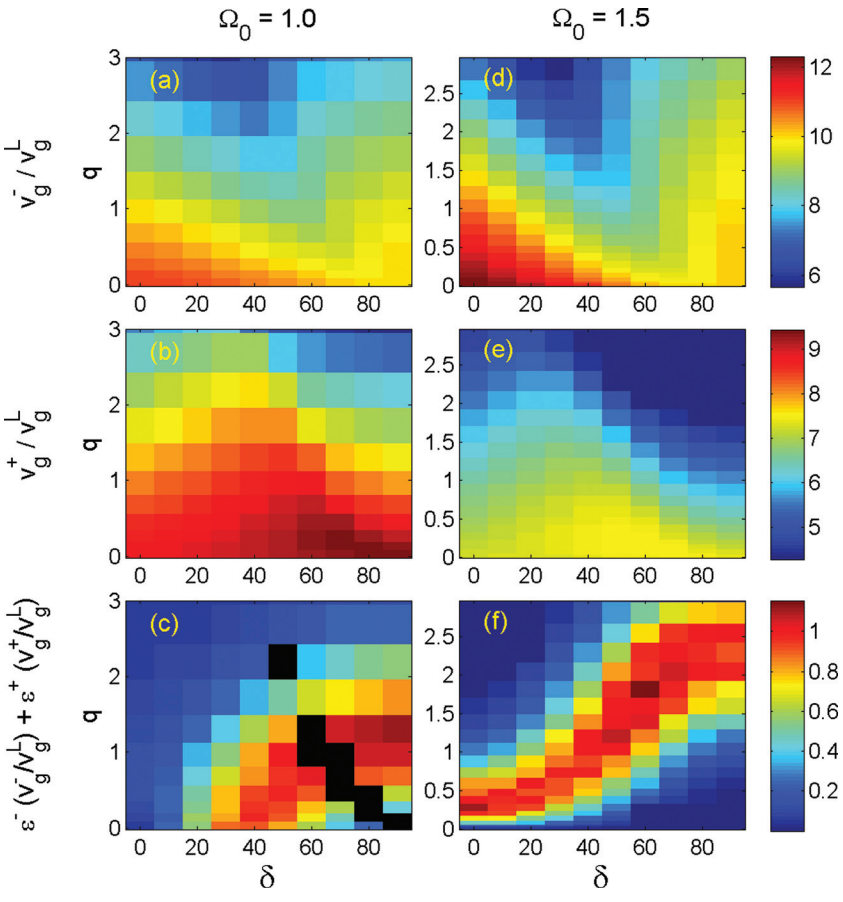

FIG. 6. For $\Omega_0 = 1.0$ and 1.5, ((a) and (b), (d) and (e)) the group velocity ratio between the *oL* (−) and *xR* (+) wave modes and Langmuir/*z* waves, ((c) and (f)) the total energy conversion efficiencies as calculated from the seperates *oL* and *xR* modes.

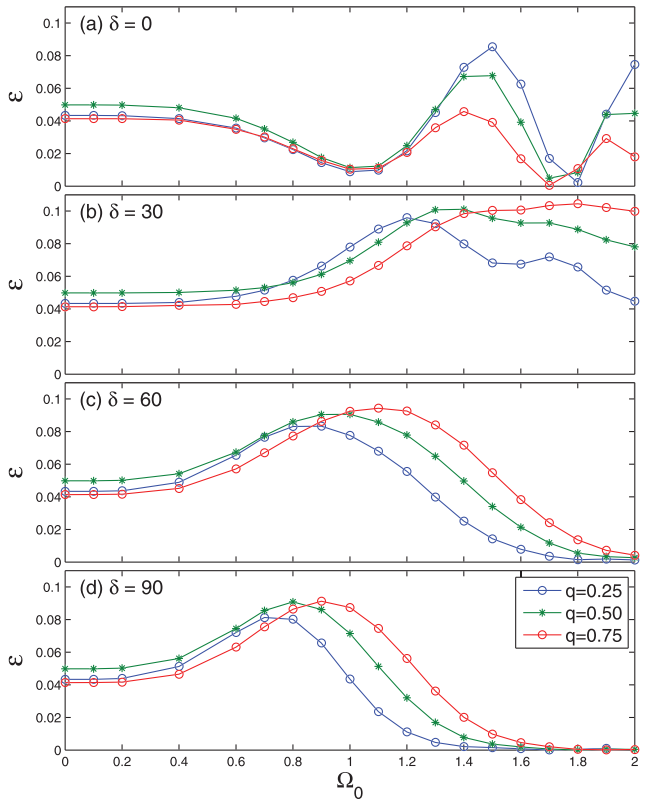

FIG. 7. Energy conversion efficiencies ε as a function of Ω_0 without separation into the oL and xR modes for q = 0.25 (blue), 0.5, (green), and 0.75 (red), respectively. The values of X_0, k_0L, and $\gamma\beta$ are as in Figures 3 and 5.

colors representing the locations $q = 0.25$, 0.5, and 0.75, respectively. The maximum conversion efficiency ε^{max} increases up to 10.4% at $\delta = 60°$ for $q = 0.75$. For $\delta = 0°$, ε^{max} occurs at $q = 0.5$, but for $\delta = 30°$–$90°$, ε^{max} occurs at $q = 0.75$. For $\delta = 0°$ in Figure 7(a), as shown by KCR08, the conversion efficiencies oscillate in Ω_0 due to interference between incoming and reflecting Langmuir/z wave modes. For $\delta = 30°$, weak oscillations are found for $q = 0.25$, but these oscillations become weaker as q increases. For $\delta = 60°$ and 90°, we found no oscillation with Ω_0. Figures 7(c) and 7(d) clearly show that ε^{max} occurs at higher Ω_0 when q increases and at lower Ω_0 when δ increases. The result for $\delta = 90°$ in Figures 3, 5, and 7 shows good agreement with the inverse LMC problems of ordinary and extraordinary waves to upper hybrid waves in cold plasma, for which Ref. 37 showed that the maximum power conversion efficiency, ε^{max}, occurs at higher Ω_0 when q increases; for instance, at $(\Omega_0, q) = (0.7, 0.8)$, (1,1), and (1.55, 1.22).

IV. DISCUSSIONS AND SUMMARY

Extending KCR08 and SCK13, we study mode conversion in warm magnetized plasmas using a numerical electron fluid simulation code where the density gradient has a wide range of angles δ to the ambient magnetic field $\mathbf{B}_0$ for a range of incident Langmuir wavevectors. One of the advantages of our wave code is that we can use it to directly determine the separate energy conversion efficiencies to oL and xR waves. Our results show that both oL and xR waves are produced for $\Omega_0 = (k_0L)^{1/3}(\omega_{ce}/\omega) < 1.5$. The xR modes are produced over a wider range, $0° \le \delta \le 90°$, for weakly magnetized plasmas with $\Omega_0 = 0.1$ and 0.7 and are produced most strongly in the range, $40° < \delta < 60°$, for intermediately magnetized plasmas with $\Omega_0 = 1.0$ and 1.5.

This finding is interesting because δ varies from 0° to 90° in space; for instance, $\delta \approx 0°$ in the solar corona, $\delta \approx 45°$ in the solar wind at 1AU,[8,26] and $\delta \approx 90°$ at the Earth's magnetic equator.[22,26] As shown in Figures 3 and 5 as well as KCR08, because the xR wave generation condition can be determined by Ω_0, KCR08 and Ref. 38 estimated the typical value of Ω_0 in various spaces such as $\Omega_{sc} \approx 0.98$ for the solar corona, $\Omega_{sw} \approx 0.87$ for solar wind at 1AU, $\Omega_{pp} \approx 1.1$–8.4 for Earth's plasmapause, $\Omega_{mp} \approx 0.2$–0.9 for magnetopause, and $\Omega_{ps} \approx 0.2$–0.6 for plasma sheet boundary layer (PSBL), respectively.

Since we adopt the typical parameters in solar wind at 1AU (except for the plasma temperature) the results thus suggest that the LMC process may play an important role in producing partially polarized solar radio emissions, especially in the solar wind at 1 AU. This result is consistent with observations of type II and III bursts with degrees of polarization between 0% and 70%.[20]

For $\delta \approx 90°$, as shown in Figure 5, the xR-mode waves can be produced for $\Omega_0 < 1.0$. Terrestrial continuum radiations, which occur for $\delta \sim 90°$, are observed as oL-mode waves[15] or both oL- and xR-mode waves.[39,40] Because $\Omega_{ps} \approx 0.2$–$0.6 < 1.0$, Schleyer *et al.*[40] expected that both oL and xR-mode waves are generated in the PSBL, which is consistent with observations.[39] Therefore, the results in this paper confirm and generalize the conclusions of KCR08 to arbitrary δ.

Similar to SCK13, both the power and energy conversion efficiencies show continuous bands in the q–δ plane for all Ω_0. For $\Omega_0 = 0.1$ and 1.5, $\varepsilon_p{}^{max}(\delta, \Omega_0)$ is relatively independent of δ, however, $\varepsilon_p{}^{max}(\delta, \Omega_0)$ increases with increasing δ for $\Omega_0 = 0.7$ and 1.0. For weakly magnetized plasmas, the total energy conversion efficiency differs from the power conversion efficiency by the ratio of the group velocity for each mode ($\varepsilon \approx \varepsilon_p \; v_g{}^L/v_g{}^{EM} \sim \varepsilon_p \; (\gamma\beta)^{1/2}$); however, in the intermediately or strongly magnetized plasmas, $\varepsilon_p/\varepsilon$ varies with δ because the ratio of group speed is different for the oL and xR modes and is a function of B_0 and δ. The maximum efficiencies $\varepsilon_p{}^{max}$ and ε^{max} increase from 50% to 99% and 5% to 14% as Ω_0 increases from 0.1 to 1.5, respectively, and the window $\Delta q_{(p)}$ becomes wider.

There are several limitations to the analysis presented in this paper. First, though Langmuir waves are more typically observed as wavepackets rather than continuous waves,[41–43] only a single continuous Langmuir wave train with constant frequency has been simulated. When wave packets propagate into the density gradient, the incoming and outgoing wavenumbers (and frequency) will vary with time and frequency and the mode conversion efficiency will vary with time and should be appropriately averaged, which is a simple generalization of Cairns and Willes.[10] Thus, the conversion should only apply to the time-average,[10,38] and the averaging further reduces the efficiency by a factor on the order of 10–30 for the solar wind and corona.

Second, a simple density gradient has been adopted in this paper. However, a Langmuir wave packet could occur in

small density fluctuations and such small-scale density fluctuations could affect wave propagation and mode conversion efficiencies. Combining a linear density profile with superposed density fluctuations, Willes *et al.*[44] found trapped modes and resonant variations in the conversion efficiency (e.g., increased efficiency when integer numbers of wavelengths fit within a cavity formed by the superposed turbulence). Recently, Yu *et al.*[45] calculated the mode conversion efficiencies from incoming EM waves to plasma oscillations in small density fluctuations shorter than wavelength and they found that a special incident angle exists at which the power mode conversion increases to almost 100% with sensitive dependences on incident parameters.

In addition, Recent STEREO observations showed that a significant number of the waveforms are consistent with trapped eigenmodes of Langmuir waves in density depletion, corresponding to waves in a potential well.[41,46,47] Because the observed eigenmodes are standing waves, they are in same ways equivalent to oppositely directed Langmuir waves, which are required for the generation of radio emission near ω_{pe} harmonic by a nonlinear process. As the trapped Langmuir waves are being reflected continuously at each side of the density well, there may also be LMC of the fundamental mode.[48,49] Therefore, the study of LMC for incoming Langmuir/z wave packets in realistic density profiles remains an interesting and important area for future work.

ACKNOWLEDGMENTS

The work at the Princeton University was supported by NASA grants (NNH09AM53I, NNH09AK63I, NNH11AQ46I, NNH11AR07I, and NNH13AV37I), NSF grants (ATM0902730 and AGS-1203299), and DOE Contract No. DE-AC02-09CH11466. The work at the University of Sydney was supported by the Australian Research Council.

[1]T. H. Stix, *Waves in Plasmas* (American Institute of Physics, New York, 1992).
[2]L. Yin, M. Ashour-Abdalla, M. El-Alaoui, J. M. Bosqued, and J. L. Bougeret, Geophys. Res. Lett. **25**, 2609–2612, doi:10.1029/98GL01989 (1998).
[3]I. H. Cairns, J. Geophys. Res. **93**, 3958–3968, doi:10.1029/JA093iA05p03958 (1988).
[4]E.-H. Kim, I. H. Cairns, and P. A. Robinson, Phys. Rev. Lett. **99**, 015003 (2007).
[5]E.-H. Kim, I. H. Cairns, and P. A. Robinson, Phys. Plasmas. **15**, 102110 (2008).
[6]F. Schleyer, I. H. Cairns, and E.-H. Kim, Phys. Plasmas **20**, 032101 (2013).
[7]R. P. Lin, D. W. Potter, D. A. Gurnett, and F. L. Scarf, Astrophys. J. **251**, 364–373 (1981).
[8]D. B. Melrose, in *Solar Radiophysics*, edited by D. J. McLean and N. R. Labrum, (Cambridge University Press, New York, 1985), p. 177.
[9]S. A. Knock, I. H. Cairns, P. A. Robinson, and Z. Kuncic, J. Geophys. Res. **106**, 25041, doi:10.1029/2001JA000053 (2001).
[10]I. H. Cairns and A. J. Willes, Phys. Plasmas **12**, 052315 (2005).
[11]D. A. Gurnett and W. S. Kurth, Space Sci. Rev. **78**, 53 (1996).
[12]J. LaBelle, Geophys. Res. Lett. **38**, L03105, doi:10.1029/2010GL046218 (2011).
[13]D. Jones, Nature **260**, 686 (1976).
[14]D. Jones, W. Calvert, D. A. Gurnett, and R. L. Huff, Nature **328**, 391 (1987).
[15]D. A. Gurnett, W. Calvert, R. L. Huff, D. Jones, and M. Sugiura, J. Geophys. Res. **93**, 12817, doi:10.1029/JA093iA11p12817 (1988).
[16]K. Rönnmark, Geophys. Res. Lett. **16**, 731, doi:10.1029/GL016i007p00731 (1989).
[17]S.-Y. Ye, J. D. Menietti, G. Fischer, Z. Wang, B. Cecconi, D. A. Gurnett, and W. S. Kurth, J. Geophys. Res. **115**, A08228, doi:10.1029/2009JA015167 (2010).
[18]P. H. Yoon, A. T. Weatherwax, T. J. Rosenberg, J. LaBelle, and S. G. Shepherd, J. Geophys. Res. **103**, 29267–29276, doi:10.1029/1998JA900032 (1998).
[19]D. B. Melrose, *Plasma Astrophysics* (Gordon and Breach, New York, 1980).
[20]G. A. Dulk and S. Suzuki, Astron. Astrophys. **88**, 203–217 (1980); see http://adsabs.harvard.edu/abs/1980A%26A....88..203D.
[21]K. G. Budden, *The Propagation of Radio Waves* (Cambridge University Press, New York, 1985).
[22]D. D. Barbosa and W. S. Kurth, J. Geophys. Res. **85**, 6729, doi:10.1029/JA085iA12p06729 (1980).
[23]J. D. Menietti, S.-Y. Ye, P. H. Yoon, O. Santolik, A. M. Rymer, D. A. Gurnett, and A. J. Coates, J. Geophys. Res. **114**, A06206, doi:10.1029/2008JA013982 (2009).
[24]W. S. Kurth, D. A. Gurnett, I. H. Cairns, D. D. Barbosa, and R. L. Poynter, Geophys. Res. Lett. **17**, 1649, doi:10.1029/GL017i010p01649 (1990).
[25]D. D. Barbosa, W. S. Kurth, S. L. Moses, and F. L. Scarf, J. Geophys. Res. **95**, 8187, doi:10.1029/JA095iA06p08187 (1990).
[26]M. G. Kivelson and C. T. Russell, *Introduction to Space Physics* (Cambridge University Press, Cambridge, United Kingdom, 1995).
[27]L. Yin and M. Ashour-Abdalla, Phys. Plasmas **6**, 449–462 (1999).
[28]E. Mjølhus, J. Plasma Phys. **30**, 179–192 (1983).
[29]M. J. Kalaee, T. Ono, Y. Katoh, M. Iizima, and Y. Nishimura, Earth Planets Space **61**, 1243 (2009).
[30]M. J. Kalaee, Y. Katoh, A. Kumamoto, T. Ono, and Y. Nishimura, Ann. Geophys. **28**, 1289 (2010).
[31]Y. Katoh and M. Iizima, Earth Planets Space **58**, e53 (2006).
[32]K.-S. Kim, E.-H. Kim, D.-H. Lee, and K. Kim, Phys. Plasmas **12**, 052903 (2005).
[33]D. W. Forslund, J. M. Kindel, K. Lee, E. L. Lindman, and R. L. Morse, Phys. Rev. A **11**, 679 (1975).
[34]A. J. Willes and I. H. Cairns, Publ. -Aston. Soc. Aust. **18**, 355–360 (2001).
[35]A. D. M. Walker, *Plasma Waves in the Magnetosphere* (Springer-Verlag, 1993).
[36]D. J. Yu, K. Kim, and D.-H. Lee, Phys. Plasmas **20**, 062109 (2013).
[37]K. Kim and D.-H. Lee, Phys. Plasmas **13**, 042103 (2006).
[38]F. Schleyer, I. H. Cairns, and E.-H. Kim, "Linear mode conversion of upper hybrid waves to radiation: Averaged energy conversion efficiencies, polarization, and applications to Earth's magnetosphere," J. Geophys. Res. (submitted).
[39]I. Nagano, S. Yagitani, H. Kojima, Y. Kakehi, T. Shiozaki, H. Matsumoto, K. Hashimoto, T. Okada, S. Kokubun, and T. Yamamoto, Geophys. Res. Lett. **21**, 2911, doi:10.1029/94GL02108 (1994).
[40]H. Matsumoto, H. Kojima, Y. Omura, and I. Nagano, in *New Perspective on the Earth's Magnetotail*, edited by A. Nishida, D. N. Baker, and S. W. H. Cowley (American Geophysical Union, Washington DC, 1998), p. 259.
[41]R. E. Ergun, D. M. Malaspina, I. H. Cairns, M. V. Goldman, D. L. Newman, P. A. Robinson, S. Eriksson, J. L. Bougeret, C. Briand, S. D. Bale, C. A. Cattell, P. J. Kellogg, and M. L. Kaiser, Phys. Rev. Lett. **101**, 051101 (2008).
[42]P. J. Kellogg, J. K. Goetz, S. J. Monson, and S. D. Bale, J. Geophys. Res. **104**, 17069, doi:10.1029/1999JA900163 (1999).
[43]D. M. Malaspina, I. H. Cairns, and R. E. Ergun, J. Geophys. Res **115**, A01101, doi:10.1029/2009JA014609 (2010).
[44]A. J. Willes, S. D. Bale, and I. H. Cairns, J. Geophys. Res. **107**, 1320, doi:10.1029/2002JA009259 (2002).
[45]D. J. Yu, K. Kim, and D.-H. Lee, Phys. Plasmas **17**, 102110 (2010).
[46]D. M. Malaspina and R. E. Ergun, J. Geophys. Res. **113**, A12108, doi:10.1029/2008JA013656 (2008).
[47]D. B. Graham and I. H. Cairns, Phys. Rev. Lett. **111**, 121101 (2013).
[48]P. J. Kellogg and D. M. Malaspina, *in The Sun, the Solar Wind, and the Heliosphere*, edited by M. P. Miralles and A. J. Sanchez (Springer, 2011).
[49]D. Malaspina, I. H. Cairns, and R. E. Ergun, Astrophys. J. **755**, 45 (2012).

The Princeton Plasma Physics Laboratory is operated
by Princeton University under contract
with the U.S. Department of Energy.

Information Services
Princeton Plasma Physics Laboratory
P.O. Box 451
Princeton, NJ 08543

Phone: 609-243-2245
Fax: 609-243-2751
e-mail: pppl_info@pppl.gov
Internet Address: http://www.pppl.gov